APPLIED SCIENCES AND ENGINEERING

Ultrastructural visualization of chromatin in cancer pathogenesis using a simple small-molecule fluorescent probe

Jianquan Xu[1], Xuejiao Sun[1], Kwangho Kim[2], Rhonda M. Brand[3], Douglas Hartman[4], Hongqiang Ma[1], Randall E. Brand[3], Mingfeng Bai[5], Yang Liu[1,3,6]*

Imaging chromatin organization at the molecular-scale resolution remains an important endeavor in basic and translational research. Stochastic optical reconstruction microscopy (STORM) is a powerful superresolution imaging technique to visualize nanoscale molecular organization down to the resolution of ~20 to 30 nm. Despite the substantial progress in imaging chromatin organization in cells and model systems, its routine application on assessing pathological tissue remains limited. It is, in part, hampered by the lack of simple labels that consistently generates high-quality STORM images on the highly processed clinical tissue. We developed a fast, simple, and robust small-molecule fluorescent probe—cyanine 5–conjugated Hoechst—for routine superresolution imaging of nanoscale nuclear architecture on clinical tissue. We demonstrated the biological and clinical significance of imaging superresolved chromatin structure in cancer development and its potential clinical utility for cancer risk stratification.

INTRODUCTION

Recent advances in superresolution fluorescence nanoscopy have transformed biological imaging as it seamlessly combines nanoscale resolution with molecular specificity. It is now routinely used in basic biological research to visualize molecular structure. However, its utility to assess clinically significant molecular structure during pathogenesis is rather limited, largely due to the lack of known targets that are of clinical significance and the technical difficulty to obtain high-quality superresolution images on the highly processed clinical samples in a robust manner.

Alteration in nuclear architecture at the microscopic scale is one of the most characteristic features in cancer cells, which is routinely examined under conventional light microscope by pathologists to diagnose cancer or determine its phenotype. Motivated by this prominent structural abnormality of chromatin in cancer cells, we aim to visualize its molecular-scale structural characteristics in malignant transformation, which cannot be easily assessed with conventional microscope. This information will be immensely valuable in understanding the pathogenesis of cancer and eventually lead to more accurate cancer detection and prognosis.

Among various types of superresolution microscopy techniques, stochastic optical reconstruction microscopy (STORM) stands out as one of the simplest yet most powerful superresolution microscopy systems because of its superior spatial resolution and the ability to use simple organic fluorophores. Our group recently improved the throughput and robustness of STORM-based superresolution microscopy and enabled robust reconstruction of superresolution images

on a widely used type of clinical samples—formalin-fixed, paraffin-embedded (FFPE) tissue, referred to as PathSTORM (1). We also identified a potential superresolved structural target as markers for cells undergoing malignant transformation—cumulative disruption in nanoscale chromatin compaction—from multiple tumor types (1).

However, the routine use of STORM in imaging chromatin on clinical samples is largely hampered by the lack of simple and reliable chromatin labels that exhibit excellent and robust photoswitching properties on the highly processed clinical tissue samples. As STORM largely depends on its ability to localize sparsely distributed single fluorescent emitters at nanometer precision, the fluorophores with fast photo-switching properties, high photon number per switching cycle, low on-off duty cycle, and low background are needed to ensure a high-quality superresolution image with minimal artifacts (2). Although many fluorophores show a certain level of photoswitching under high-power density of the illumination laser, Alexa Fluor 647 or its close structural analog cyanine 5 (Cy5) remains the gold standard for STORM imaging, yielding the best image quality and highest resolution (2). However, these organic fluorophores cannot spontaneously target DNA in the cell or tissue, so immunofluorescence is the most commonly used method to label chromatin with Alexa647 or Cy5 conjugated with antibodies that recognize chromatin proteins (e.g., core histones, histone posttranslational modifications). However, this approach relies on the quality of antibody that often lacks consistency, limiting its routine clinical use. On the other hand, small-molecule DNA binding fluorescent dyes such as Hoechst or 4′,6-diamidino-2-phenylindole (DAPI) are the most widely used fluorophores for staining genomic DNA in clinical and preclinical tissue samples. They are fast, specific to DNA with high staining efficiency, low cost, fluorogenic, and easy to use without the need of multiple washing steps as in immunofluorescence staining. However, current small-molecule DNA stains do not have optimal blinking properties for robust and high-quality STORM-based superresolution imaging.

The ideal DNA label for STORM imaging is a small-molecule DNA label that efficiently and spontaneously binds to DNA with

[1]Biomedical Optical Imaging Laboratory, Departments of Medicine and Bioengineering, University of Pittsburgh, Pittsburgh, PA 15213, USA. [2]Department of Chemistry, Vanderbilt Institute of Chemical Biology, Vanderbilt University, Nashville, TN 37232, USA. [3]Department of Medicine, Division of Gastroenterology, Hepatology, and Nutrition, University of Pittsburgh, Pittsburgh, PA 15213, USA. [4]Department of Pathology, School of Medicine, University of Pittsburgh School of Medicine, Pittsburgh, PA 15213, USA. [5]Department of Radiology and Radiological Sciences, Vanderbilt University Medical Center, Nashville, TN 37232, USA. [6]University of Pittsburgh Hillman Cancer Center, Pittsburgh, PA 15232, USA.
*Corresponding author. Email: liuy@pitt.edu

excellent photoswitching properties for STORM imaging. Hoechst tagging to a fluorophore of interest has been introduced as a modular strategy for live-cell nucleus fluorescence imaging (3, 4). For example, Hoechst conjugated with carboxylated silicon–rhodamine (SiR) (5) and rhodamine (6) has been used for stimulated emission depletion–based superresolution imaging of DNA in live cells. Hoechst conjugated with Janelia Fluor dyes were also used for superresolution imaging of DNA in live cells based on point accumulation for imaging in nanoscale topography (7, 8) or STORM (9). However, these conjugates prioritize the need for live-cell DNA imaging on cell culture with suboptimal photoswitching performance best suited for STORM imaging on highly processed clinical tissue. Inspired by Hoechst tagging strategy, we conjugated one of the best-performing organic dyes for STORM, Cy5, with Hoechst as a simple and fast small-molecule DNA label for high-quality STORM imaging of genomic DNA on clinical tissue sections. We validated Hoechst-Cy5 for STORM imaging of chromatin structure on clinically prepared FFPE tissue section and benchmarked its performance against several small-molecule DNA fluorescent stains that were attempted for STORM imaging as well as traditional immunofluorescence staining. We further demonstrated the significance of superresolution imaging of molecular composition and structural characteristics of nuclear architecture in malignant transformation, which were not visible under conventional light microscopy in three applications: imaging cumulative disruption of chromatin compaction at different stages of colon carcinogenesis, two-color superresolution imaging of chromatin nanodomains and transcriptional machinery or nuclear lamina, and cancer risk stratification from normal-appearing colon tissue. These results not only demonstrated the robust performance of STORM imaging on clinical samples but also provided strong evidence for biological and clinical significance of imaging superresolved nuclear architecture beyond conventional microscopic assessment in cancer research.

RESULTS

Validation of Hoechst-Cy5 for STORM-based superresolution imaging of genomic DNA in clinically prepared tissue

To take advantage of the excellent photoswitching properties of Cy5 for high-quality STORM imaging of genomic DNA and DNA binding capability of Hoechst, a small molecule dye, we developed Hoechst-Cy5 conjugate by first synthesizing a conjugable analog of Hoechst, followed by bioconjugation with Cy5 (for synthetic routes, detailed steps, and validation, see fig. S1 and Supplementary Materials and Methods). As shown in Fig. 1, the absorption spectrum of Hoechst-Cy5 showed the absorption for both Hoechst (around 365 nm) and Cy5 (around 650 nm), and their emission spectra showed emission peaked around 460 and 660 nm (Fig. 1B). When excited at 642 nm, Hoechst shows negligible fluorescence intensity compared with that of Cy5 and provided low background for STORM imaging of
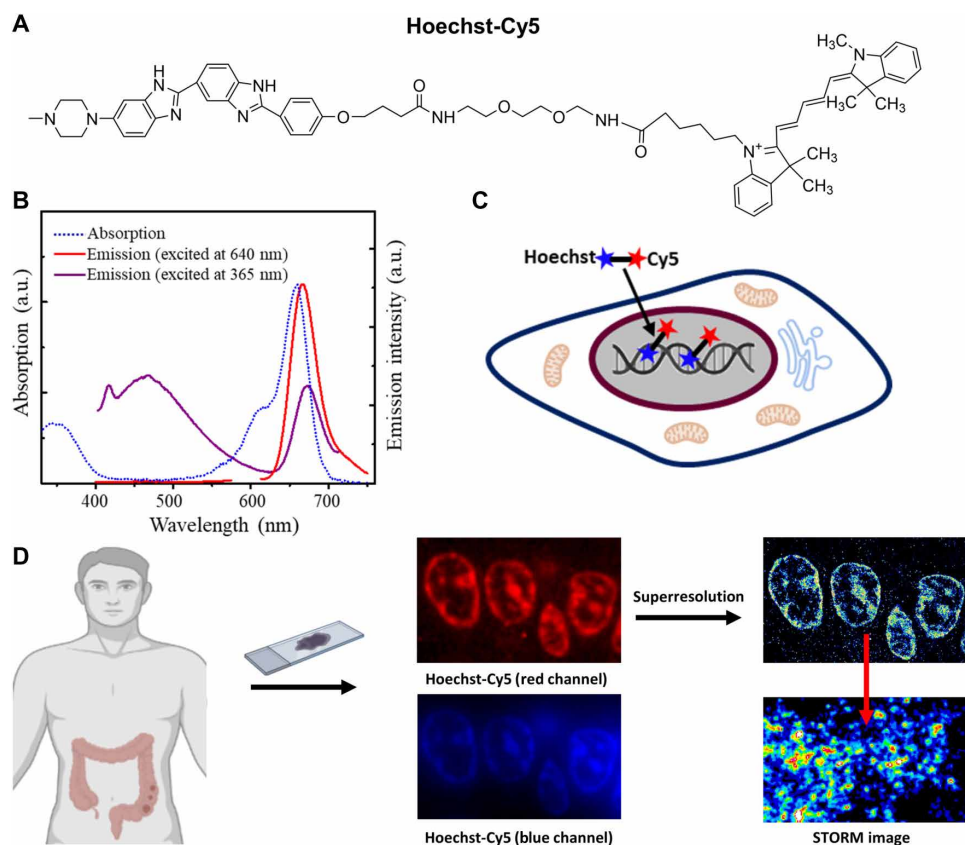

Fig. 1. Schematic illustration of Hoechst-Cy5 for superresolution imaging of genomic DNA on clinical tissue. (**A**) Chemical structure of Hoechst-Cy5. (**B**) Absorption spectra and emission spectra excited at 365 and 642 nm. a.u., arbitrary unit. (**C**) Schematic illustration of the Hoechst tagging strategy for DNA labeling with Cy5. (**D**) Schematic illustration of superresolution imaging of chromatin structure on pathological tissue for disease assessment.

Cy5 channel. Their wide-field fluorescence image of tissue nuclei excited at 405 nm (for Hoechst) showed a good agreement (Pearson's r value = 0.87) with that excited at 642 nm (Fig. 1D), suggesting that DNA was successfully labeled with Cy5 by its conjugation with Hoechst. Superresolution image of DNA can be obtained through STORM imaging of Cy5.

We then benchmarked the performance of Hoechst-Cy5 for STORM imaging of genomic DNA using tissue section of mouse intestinal tissue prepared with standard clinical protocol (formalin-fixed and paraffin-embedded), against three other small-molecule DNA binding dyes that were attempted and optimized for localization-based superresolution imaging, including TOTO-3 Iodide (TOTO-3) (1), NucSpot Live 650 (Live-650) (10), and Hoechst Janelia Fluor 646 (Hoechst-JF646, a gift from L. Lavis) (7, 8). Staining or imaging condition for each dye was optimized by adjusting concentration and imaging buffer to achieve the optimal image quality (see Methods
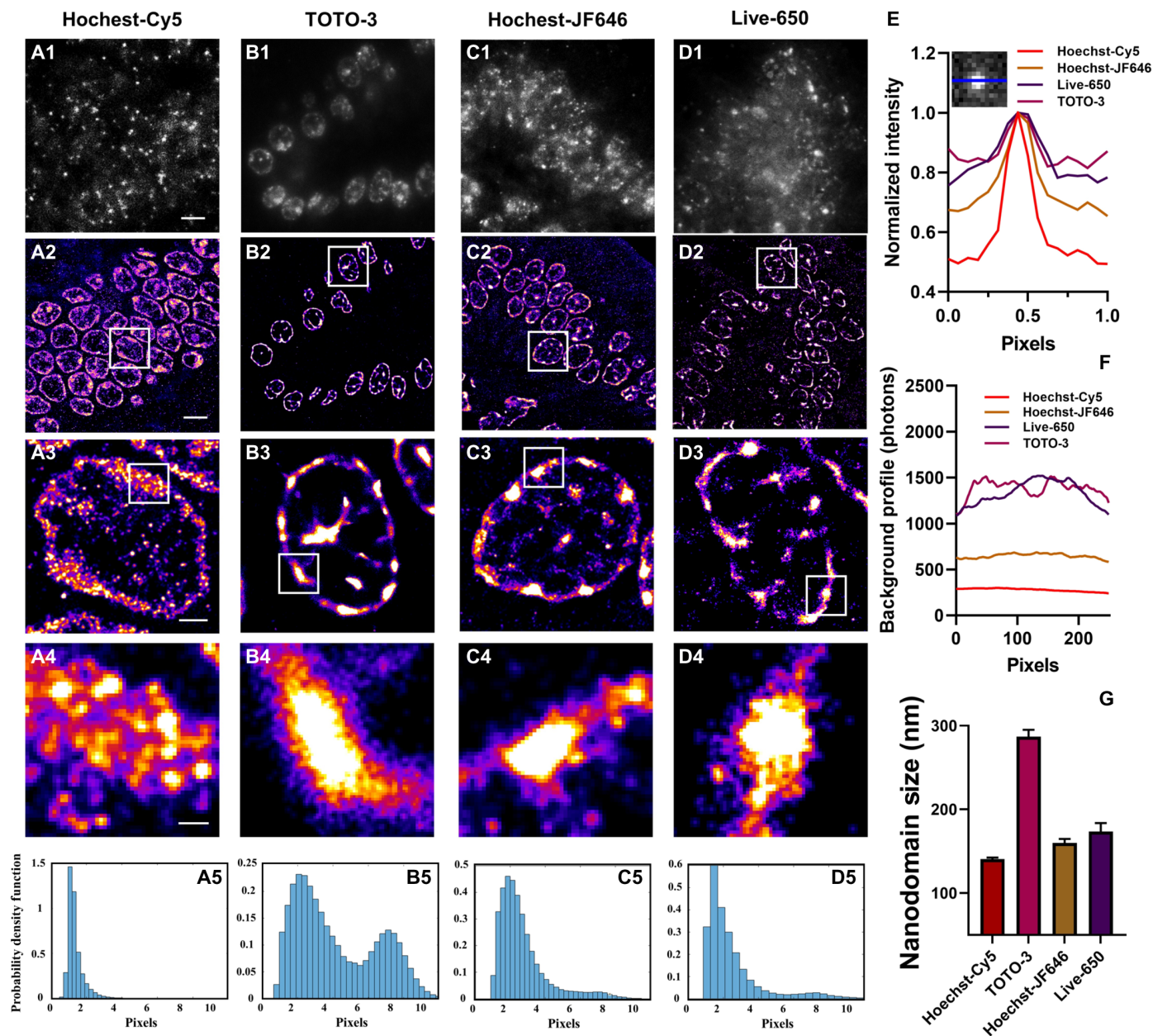

Fig. 2. Performance comparison of DNA dyes for STORM imaging on FFPE tissue section. (**A1** to **D1**) Single-frame raw image of DNA labeled with Hoechst-Cy5, TOTO-3, Hoechst-JF646, and Live-650. (**A2** to **D2**) Superresolution images of genomic DNA stained with different dyes reconstructed with ThunderSTORM, from normal intestinal mouse tissue. (**A3** to **D3** and **A4** to **D4**) Progressively zoomed regions of superresolution images from A2 to D2. Scale bars, 5 μm, 1 μm, and 200 nm in the original and magnified images, respectively. (**A5** to **D5**) Histogram distribution of SD (sigma) of individual emitters from Gaussian fitting using ThunderSTORM ImageJ plugin. The emitters with the fitted sigma value of larger than two pixels are considered as overlapping emitters. (**E**) Normalized line profiles across the emitter spots demonstrate the signal-to-noise ratio. Inset: An example of line profile. (**F**) Average background profiles estimated for each small-molecule DNA probe on the raw images. (**G**) The DNA nanodomain size calculated from the STORM images using four different DNA stains (n = 61, 53, 64, and 56 cells, respectively).

and Materials for details). Figure 2 shows the comparison of a single-frame raw image of genomic DNA labeled with Hoechst-Cy5 and three other DNA dyes (for image stacks, see "Data and materials availability" section for details), respectively. The raw images from Hoechst-Cy5 (Fig. 2A1) showed the lowest background with highest signal-to-background contrast, sparse, and well-separated emitters. In comparison, the other three dyes are more difficult to bleach with significantly more overlapping fluorescent emitters, which increase the background (Fig. 2, B1 to D1). The average background and line profile across the emitters for each fluorophore are shown in Fig. 2 (E and F). The presence of overlapping emitters is a major factor compromising the image resolution in localization-based super-resolution imaging. To estimate the contribution of overlapping emitters to the reconstructed image, Fig. 2 (A5 to D5) shows the distribution of the SD (sigma) of individual emitters obtained from Gaussian fitting with ThunderSTORM ImageJ plugin (11), which is an indicator of overlapping emitters. It shows that Hoechst-Cy5 has ~7% of localized emitters with sigma larger than two pixels (considered as overlapping emitters), while TOTO-3, Live-650, and Hoechst-JF646 exhibited approximately 81, 64, and 47%, respectively.

The quality of the raw data directly affects the subsequent image resolution and quantitative analysis of superresolved chromatin structure. As shown in Fig. 2A, the high-signal, low-background, and well-separated molecules from Hoechst-Cy5 result in the STORM images with the best-resolved DNA nanodomains (Fig. 2, A3 and A4) compared with those with the other three dyes (Fig. 2, B3 to D3 and B4 to D4). The subsequent calculation of DNA nanodomain size in Fig. 2E further confirmed the above observation of chromatin structure, where the analysis of superresolution images from Hoechst-Cy5 showed the smallest nanodomain size, consistent with the best-resolved chromatin nanodomains in the STORM images.

To further improve the image resolution, we applied our previously developed PathSTORM (1) to account for the nonuniform background and the small percentage of overlapping emitters. As shown in fig. S2, PathSTORM image reconstruction algorithm improved the overall image quality for all fluorophores, but the STORM image from Hoechst-Cy5 remains the best. Therefore, all of the subsequent STORM image reconstructions were performed with PathSTORM unless otherwise stated.

Recognizing that Hoechst binds to AT-rich sequences, to further validate the superresolution image of genomic DNA labeled by Hoechst-Cy5 truly reflects the structure of genomic DNA in tissue, we compared the STORM images of genomic DNA labeled using Hoechst-Cy5 with both condensed heterochromatin regions marked by H3K9me3 and open euchromatin regions marked by H3K4me3 that were labeled using immunofluorescence staining without sequence specificity. As shown in Fig. 3, the condensed region of genomic DNA largely overlaps with H3K9me3, and the open region overlaps well with H3K4me3. This result further confirms the structural integrity of genomic DNA labeled by Hoechst-Cy5 at the level of resolution of STORM imaging.

Superresolution imaging of genomic DNA in normal and pathological tissue

Imaging molecular-scale chromatin structure in tissue with well-preserved spatial context is especially important, as tissue is often heterogeneous with various cell types and mixed pathological entities. Using Hoechst-Cy5 and STORM imaging, we first assessed the nanoscale chromatin structure from different cell types of intestinal tissue, including intestinal stem cells, intestinal epithelial cells, and immune cells, where each cell type was identified with cell type–specific markers or morphological locations. As shown in Fig. 4, the
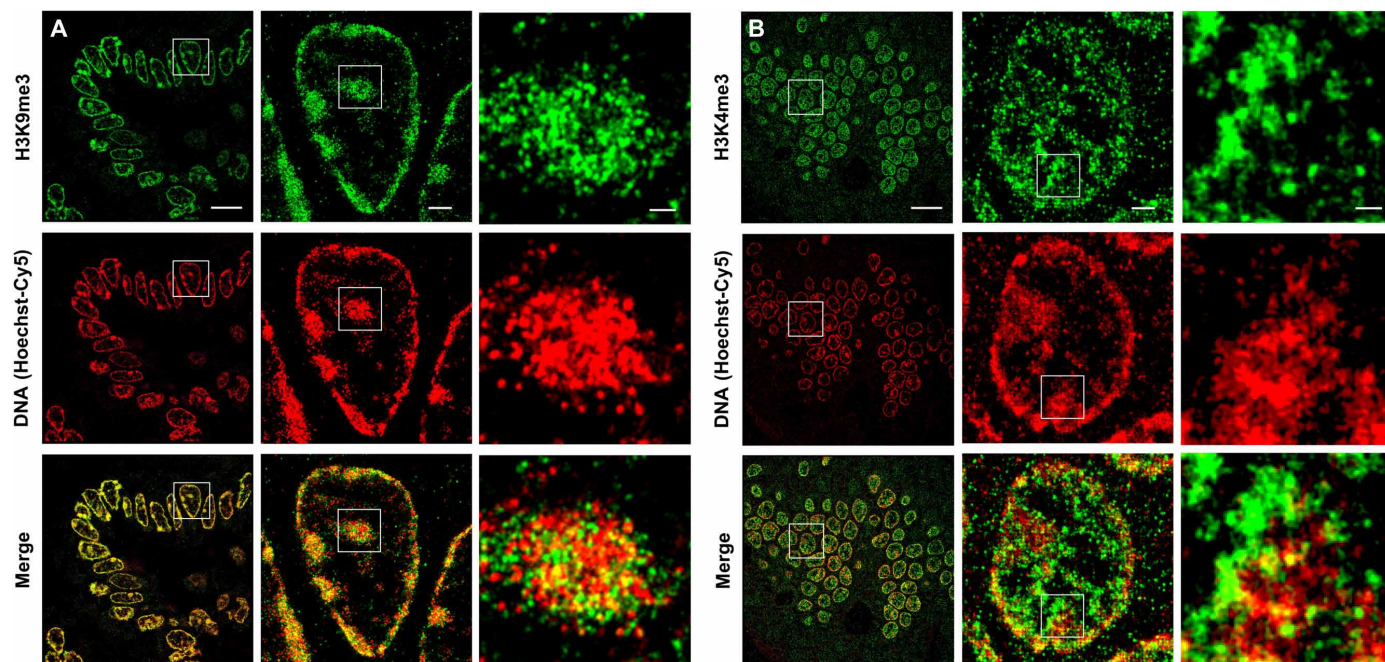

Fig. 3. Two-color superresolution images of DNA and histone marks on mouse intestinal tissue. (**A**) Representative two-color STORM images showing the spatial relationship between DNA and heterochromatin regions marked by H3K9me3. (**B**) Representative two-color STORM images showing the spatial relationship between DNA and euchromatin regions marked by H3K4me3. Scale bars, 10 μm, 1 μm, and 200 nm in the original and magnified images, respectively.
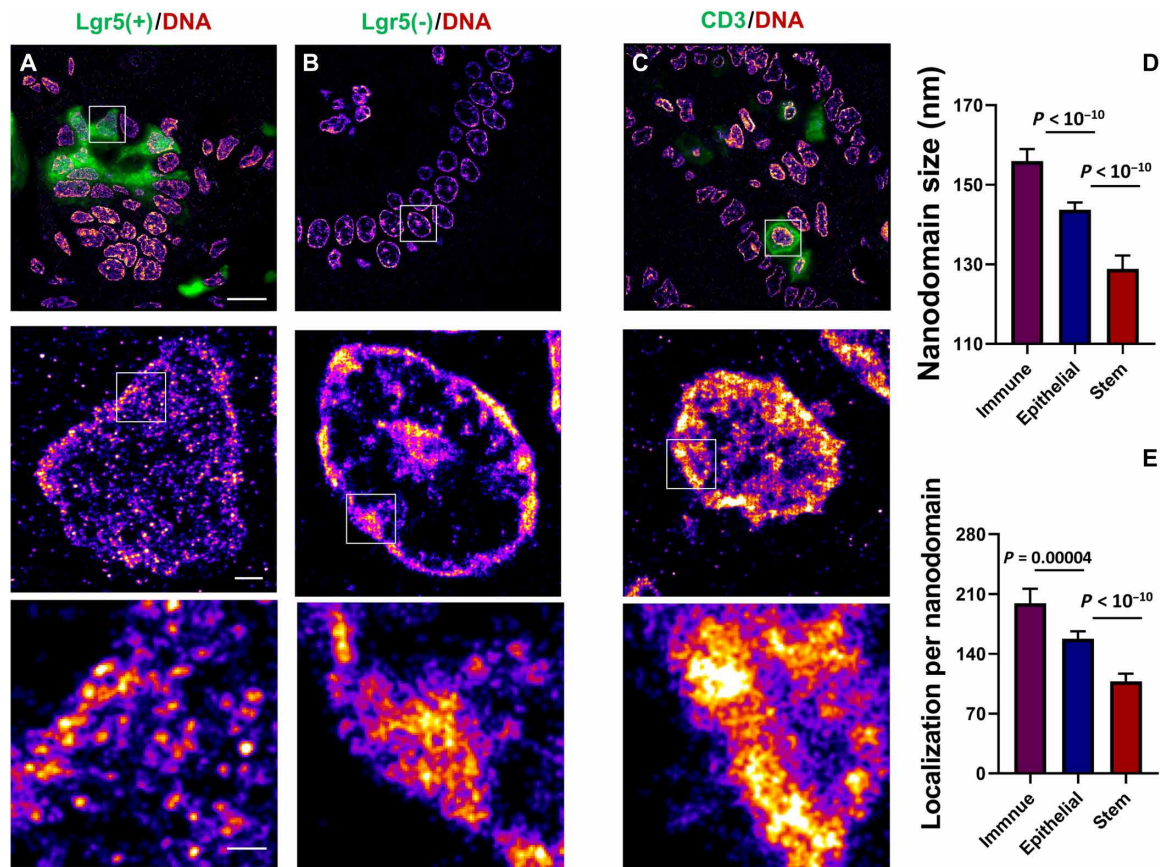
Fig. 4. Superresolution imaging of genomic DNA in different cell types from mouse intestinal tissue. (**A** and **B**) Superresolution images of DNA from intestinal stem cells (Lgr5 positive) and differentiated cell in the villi region (Lgr5 negative). (**C**) Superresolution images of DNA from immune cells marked by CD3. Scale bars: 10 and 1 μm in the original and magnified images, respectively. (**D** and **E**) Statistical analysis of the DNA nanodomain size and number of localizations per nanodomain for each group, and the numbers of nuclei analyzed were n = 73, 87, and 58, respectively.

STORM images clearly showed heterogeneous nanodomains formed by genomic DNA, consistent with the previous reports (*1*, *12*). Three different cell types exhibited distinct structural characteristics in chromatin compaction. Intestinal stem cells (marked by Lgr5) assumed more open compaction over the entire nucleus (Fig. 4A), supporting the previous report that ground-state pluripotent stem cells had less dense clutches containing fewer nucleosomes and nucleosome clutch size strongly correlated with their pluripotency (*12*). Epithelial cells located in the villi region of the intestinal tissue showed more condensed and clumpy regions, but both open and condensed regions are well delineated in the nucleus (Fig. 4B). Immune cells (T cells marked by CD3) exhibit the most compact chromatin structure among the three cell types (Fig. 4C), consistent with the fact that immune cells are mostly maintained in their quiescent (resting) state. Quantitative analysis of nanodomain size and localizations per nanodomain formed by DNA further support their structural distinction.

Next, we focused on intestinal epithelial cells as they are the most diagnostically significant. We evaluated their nanoscale chromatin structure from normal, precancerous, and cancerous tissue of human colon from the clinically collected FFPE tissue blocks. Samples from four patients from each group with a total of 12 patients were analyzed. Figure 5 shows the hematoxylin and eosin–stained histology images and the superresolution STORM images of genomic DNA

in colon epithelial cells. At the microscopic scale, nuclear architecture from precancerous and cancerous tissues showed irregular shape and distinct chromatin texture compared with normal epithelial cells. While superresolution images of genomic DNA show characteristic DNA nanodomains from three distinct stages of colorectal carcinogenesis. In normal cells, chromatin nanodomains are most compact, especially at the nuclear periphery. At precancerous stage, chromatin compaction shows slight disruption. In most cancer cells, the compact chromatin structure is significantly disrupted, mostly prominent at nuclear periphery, where the highly compact chromatin at nuclear periphery is indistinguishable from that at the interior of the nucleus. Of note, this structural disruption in compact chromatin cannot be easily detected using conventional fluorescence microscopy (fig. S3). Overall, the nanodomain size of genomic DNA became progressively smaller during colorectal carcinogenesis, corresponding to more disrupted chromatin compaction (Fig. 5, D and E). This result is consistent with our previous finding that heterochromatin marked by H3K9me3 was progressively disrupted in precancerous and cancerous lesions in human colon tissue (*1*).

Two-color superresolution imaging of genomic DNA and nuclear proteins in normal and pathological tissue
Chromatin compaction directly affects many cellular processes, and two-color superresolution imaging between chromatin compaction
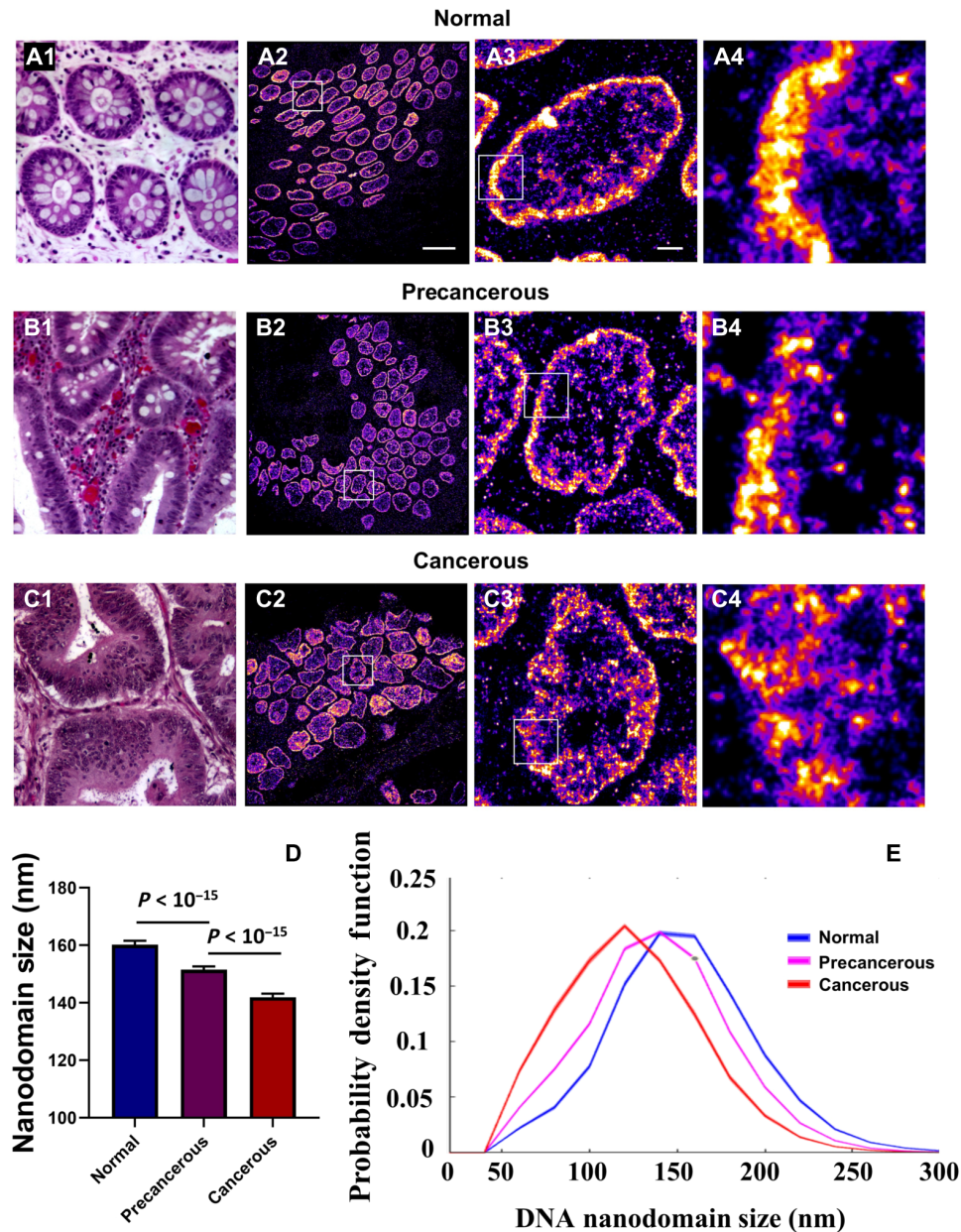
Fig. 5. Superresolution imaging of genomic DNA in normal and pathological tissue. (**A1** to **C1**) Representative hematoxylin and eosin (H&E)–stained histology images of the colorectal tissue from normal, precancerous (low-grade dysplasia/adenoma), and cancerous (adenocarcinoma) lesions. (**A2** to **C2**, **A3** to **C3**, and **A4** to **C4**) Representative superresolution images of DNA and progressively zoomed regions from (A1) to (C1). Scale bars, 10 μm, 1 μm, and 200 nm in the original and magnified images, respectively. (**D**) Statistical analysis of the DNA nanodomain size for each group. (**E**) Probability density function of the average DNA nanodomain size with each nucleus for each group and $n = 192, 148,$ and 152 cells from a total of 12 patients (4 patients per group), respectively.

and functionally important nuclear proteins provides key insights into the underlying molecular composition of nuclear architecture. Transcription is a fundamental cellular process regulated by chromatin organization and generally up-regulated in cancer cells to maintain the enhanced metabolism and other cellular activities in cancer cells (*13*, *14*). As chromatin compaction directly affects the transcriptional machinery, we first examined the nanoenvironment of chromatin compaction in normal and pathological colon tissue using two-color STORM imaging of genomic DNA and active RNAPII. As shown in Fig. 6, active RNAPII nanoclusters are largely

overlapped with the open regions of DNA, where the condensed nuclear periphery shows no enrichment of active RNAPII. As expected, the nanoclusters formed by active RNAPII become larger in precancerous and cancerous tissues (Fig. 6D), consistent with the increased transcription activities in cancer cells (*1*). The degree of colocalization between active RNAPII nanoclusters and genomic DNA is also increased (Fig. 6E), suggesting possible interaction between them.

Nuclear membrane irregularity is another common morphologic finding in cancer cells (*15*). Intrigue by the above observation of
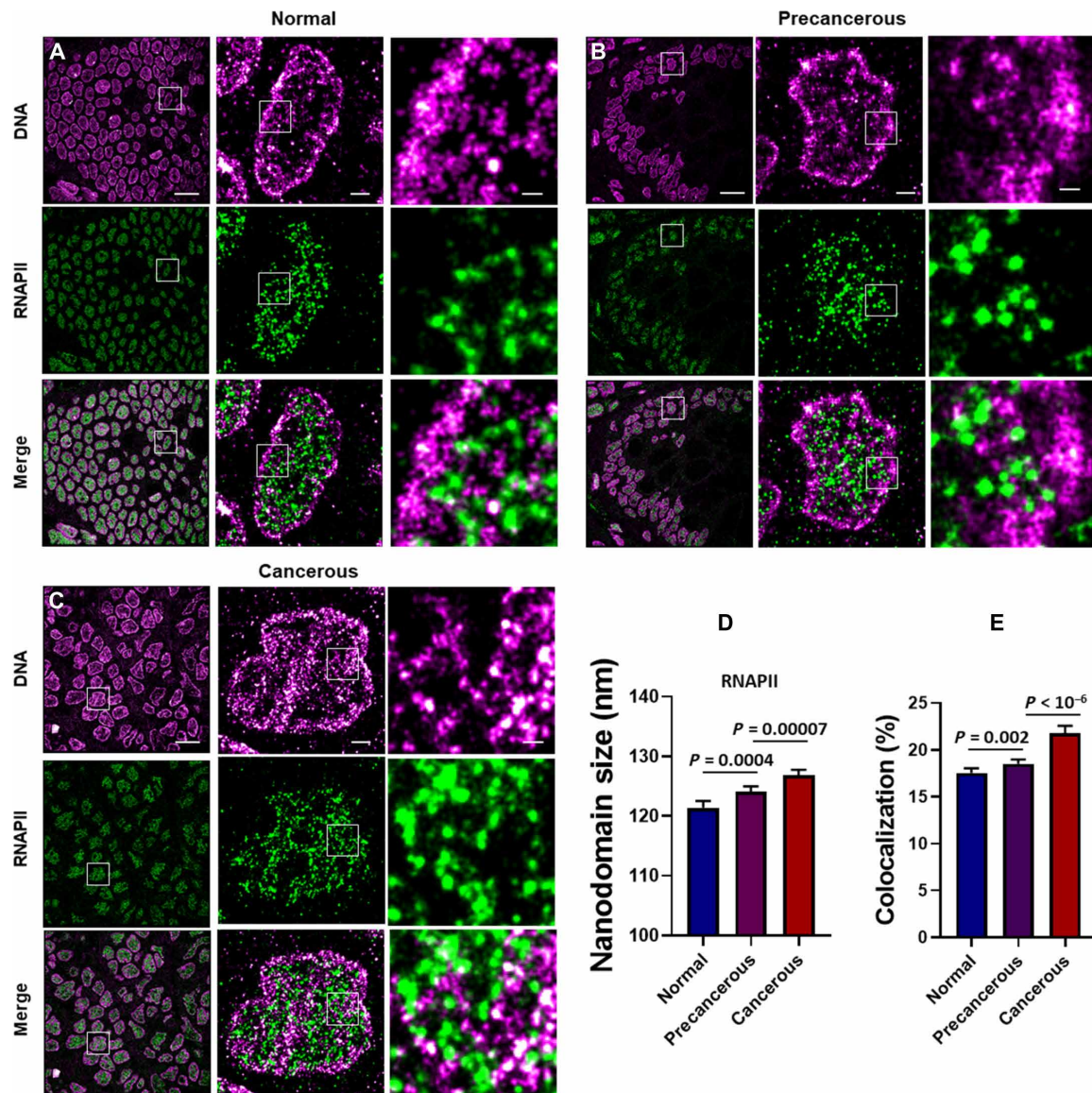
Fig. 6. Two-color superresolution imaging of genomic DNA and RNAPII in normal and pathological tissue. (**A** to **C**) Two-color STORM images of genomic DNA and RNAPII from normal patient and patients with precancerous (low-grade dysplasia/adenoma) and cancerous (adenocarcinoma) lesions. Scale bars, 10 μm, 1 μm, and 200 nm in the original and magnified images, respectively. (**D**) Statistical analysis of the RNAPII nanodomain size for each group. (**E**) Degree of colocalization between genomic DNA and RNAPII; the numbers of cells analyzed were $n = 129$, 139, and 164 from a total of 12 patients (4 patients per group), respectively.

significantly disrupted chromatin compaction at the nuclear periphery of cancer cells, we further examined the superresolved structure and physical association between nuclear lamina and chromatin on human colon pathological tissue. Nuclear lamina is a meshwork of intermediate filaments that are physically associated with condensed heterochromatin [referred to as lamina-associated domains (LADs)], providing links among the genome, nucleoskeleton, and cytoskeleton (*16*, *17*). Altered expression level and/or localization of lamins have been reported in different types of tumors including colorectal cancer (*18–20*). Studies have also demonstrated the disruption of LADs and alteration in the epigenome in cancer (*21*). Figure 7 shows the two-color superresolution images of chromatin and nuclear lamina (marked by lamin A/C) in normal, precancerous, and cancerous tissues from human colon. In normal colonic epithelial tissue (Fig. 7A),

nuclear lamina shows continuous borders tethered to the condensed chromatin at the nuclear periphery. The cross-sectional profile shows well-separated nuclear lamina regions and condensed chromatin regions (Fig. 7D). In precancerous tissue (Fig. 7B), the disrupted chromatin compaction at the nuclear periphery is associated with more fragmented nuclear lamina lining at the nuclear periphery, with some spatial overlapping between nuclear lamina and chromatin (Fig. 7E). In cancer tissue (Fig. 7C), a more significant physical association can be seen between severely fragmented chromatin nanodomains and nuclear lamina. Overall, there is a progressively increased colocalization between nuclear lamina and chromatin regions located at the nuclear periphery, as shown in Fig. 7G. In addition, the nanodomain size from chromatin and nuclear lamina is progressively reduced in precancerous and cancer cells, and their sizes were positively

correlated (Fig. 7H). This spatial association between the two nano-domains supports the significance of lamina-associated chromatin domain in cancer. We also noticed a significant level of heterogeneity for both chromatin and lamina structures in cancer tissue. Although most cancer cells show severe disruption of chromatin compaction and nuclear lamina, a small fraction of the cancer cells still maintain relatively intact or less disruptive structure (fig. S4), which may be protected from drug exposure and resistant to treatment (22).

Superresolution imaging of genomic DNA in cancer risk stratification

We next explore whether superresolution imaging of genomic DNA can be used to detect cancer beyond conventional pathological assessment of tumor tissue. As a proof of concept, we assessed its ability to stratify cancer risk of patients with well-defined cancer risk. Given that the patients had no colon cancer at the time of the study, we analyzed their normal-appearing tissue biopsies. Patients with Lynch syndrome represent a well-established high-risk cohort with significantly increased risk of developing colorectal and endometrial cancers and certain other types of cancer (23). Three groups of patients with increasing cancer risk were evaluated, including healthy controls; unaffected Lynch, defined as patients with a germline DNA mismatch repair mutation but without a past history of cancer; and affected Lynch, defined as patients with a germline mismatch repair mutation and a past history of colorectal cancer. None of them presented with tumor at the time of colonoscopy, and the normal-appearing colon tissue was biopsied. As shown in Fig. 8, both STORM images of genomic DNA and the quantitative analysis
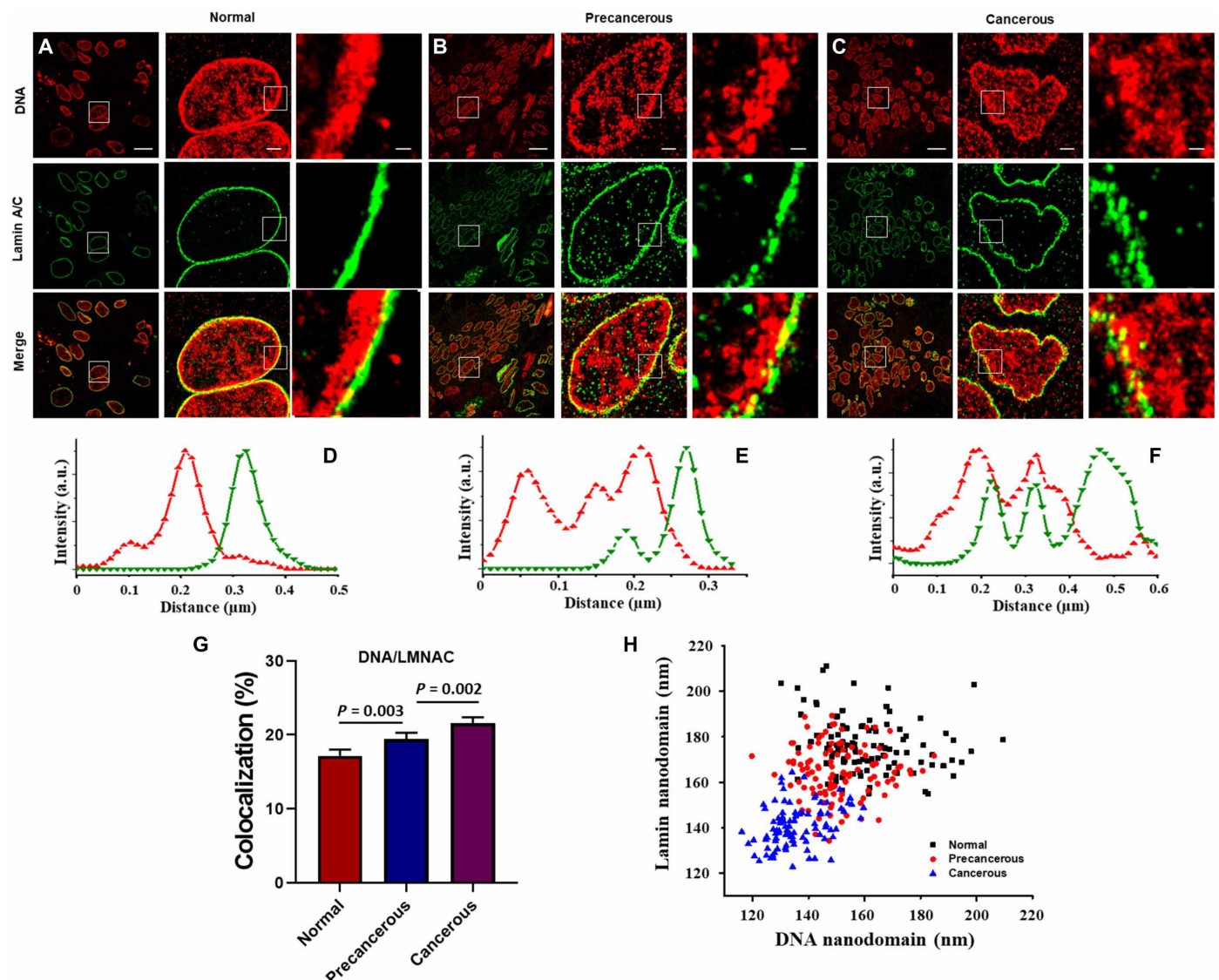

Fig. 7. Two-color superresolution imaging of genomic DNA and nuclear lamina in normal and pathological tissue. (**A** to **C**) Two-color STORM images of genomic DNA and lamin A/C from normal patients and patients with precancerous (low-grade dysplasia/adenoma) and cancerous (adenocarcinoma) lesions. Scale bars, 10 μm, 1 μm, and 200 nm in the original and magnified images, respectively. (**D** to **F**) Intensity profile showing the spatial relationship between DNA and lamin A/C at the nuclear periphery. (**G**) Degree of colocalization between genomic DNA and lamin A/C (LMNAC) at the nuclear periphery. (**H**) Correlation between the nanodomain sizes formed by genomic DNA and lamin A/C (Pearson's $r = 0.48$, $P < 10^{-10}$); the numbers of nuclei analyzed were $n = 101$, 113, and 95 from a total of 12 patients (4 patients per group), respectively.
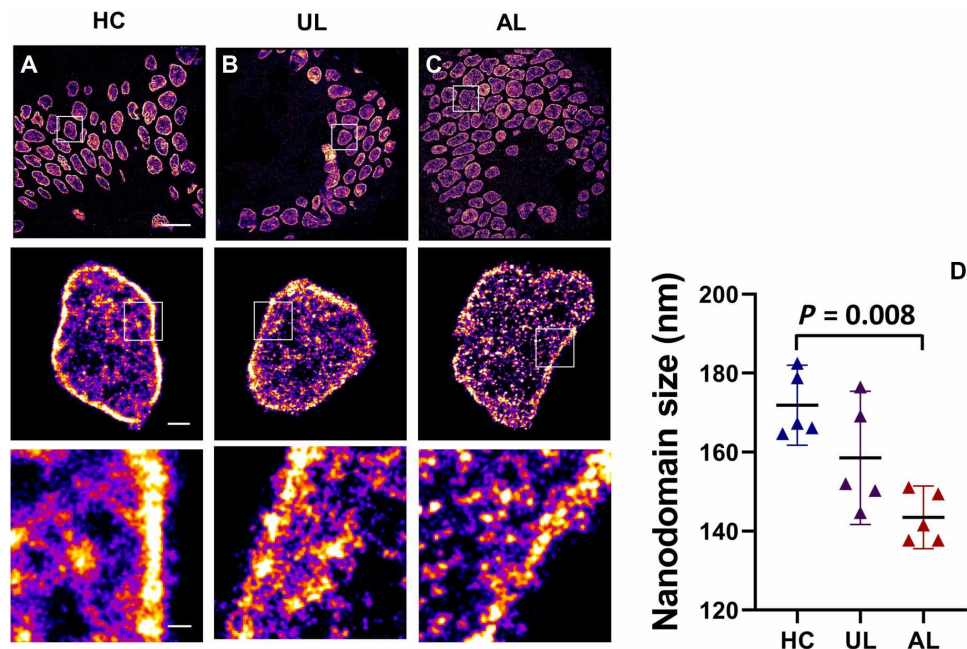
Fig. 8. Superresolution imaging of genomic DNA for cancer risk stratification. (**A** to **C**) Representative superresolution images of DNA of colon tissue biopsies from patients of healthy controls (HCs), unaffected Lynch (UL) patients, and affected Lynch (AL) patients. All biopsies were from transverse colon, obtained endoscopically, processed with standard formalin fixation and paraffin embedding. Scale bars, 10 μm, 1 μm, and 200 nm in the original and magnified images, respectively. (**D**) Average DNA nanodomain size in three patient groups from a total of 15 patients. Each point is the average from over 100 cell nuclei for each patient.

of DNA nanodomain size show significantly more open chromatin or disrupted compaction in the cell nuclei of normal-appearing colonic epithelial tissue in affected Lynch patients compared with healthy controls, suggesting that the disrupted chromatin structure can occur in normal cells at risk for carcinogenesis. On the other hand, chromatin compaction from unaffected Lynch patients shows a larger spread between those of healthy controls and affected Lynch patient group, with some resembling the healthy controls and some resembling the affected Lynch patients, which may be associated with the penetrance of genetic predisposition. Overall, this result not only reveals the presence of disrupted chromatin compaction in the normal cells in patients with increasing cancer risk but also suggests the potential of superresolution chromatin imaging for cancer risk stratification from nontumor cells.

DISCUSSION

Direct visualization of nanoscale nuclear architecture and chromatin compaction on pathological tissue is of immense importance in cancer research, from basic discovery of nanoscale molecular structure in cancer pathogenesis to translational research for identifying new biomarkers for improving cancer detection. The small-molecule fluorescent probe as a simple and fast DNA stain presented in this work will facilitate the routine use of superresolution chromatin imaging to visualize molecular-scale nuclear architecture, especially on FFPE clinical tissue samples.

Several strategies have been developed for STORM imaging of genomic DNA or chromatin. In dSTORM imaging, Cy5 or Alexa647 remains the gold standard, so the best strategy for STORM imaging often incorporates Cy5 or Alexa647 with the labeling target. A common method is using the azide derivative of Cy5 or Alexa647 to

detect 5-ethynyl-2′-deoxyuridine (EdU) based on a click reaction, which is incorporated into DNA during active DNA synthesis on live cells (24, 25). Since EdU is only incorporated into the newly synthesized DNA, an entire cell cycle is often required to fully label genomic DNA, and the labeling efficiency is also affected by the cell cycle status or proliferation rate. As shown in fig. S5, some cells without newly synthesized DNA during the labeling cycle were not labeled, while some cells with various proliferation rates showed different labeling efficiency or chromatin structure. Furthermore, this method is not applicable for cells without proliferation, such as primary cells or clinically processed patient samples. Therefore, instead of directly labeling DNA, immunofluorescence staining using antibodies against DNA-associated proteins conjugated with Alexa647 or Cy5 is often used for STORM imaging of chromatin in fixed cells and tissue (1, 12). However, this approach highly depends on the quality of the antibody, which can vary between batch to batch and usually require time-consuming antigen retrieval, staining, and washing steps.

The most popular choice for direct labeling of DNA is small-molecule DNA-intercalating or DNA-binding dyes such as TOTO-3 (1), Live-650 (10), YOYO-1 (26), SYTO (27), and Hoechst (28), although some (e.g., TOTO-3 and SYTO) also bind to RNA, which requires additional ribonuclease (RNase) digestion. As most fluorophores exhibit different levels of blinking properties under high laser power density and optimized imaging buffers (2), these small-molecule DNA stains have been used for STORM imaging of DNA in cultured cells with mixed success. However, none of them are well suited for STORM imaging of chromatin on clinical FFPE tissue section. As shown in Fig. 2, suboptimal photoswitching properties of the conventional small-molecule DNA fluorophores in tissue introduce high and nonuniform background and overlapping emitters,

which significantly reduce image resolution and introduce serious artifacts.

In this work, by covalently linking one of the best-performing organic dyes (Cy5) for STORM with a commonly used small-molecule DNA-binding probe (Hoechst), we demonstrated that Hoechst-Cy5 achieved superior photoswitching performance for STORM imaging of chromatin on clinically prepared FFPE tissue section for robust and high-quality localization-based superresolution imaging. Given that FFPE tissue blocks represent a large resource of human tissue (29), Hoechst-Cy5 facilitates routine examination of chromatin ultrastructure that underlies various clinical conditions. In addition, Hoechst-Cy5 can also be used for superresolution imaging of genomic DNA in cell culture (fig. S6). For example, by combining Hoechst-Cy5 staining of genomic DNA with pulse labeling with EdU, we can visualize the spatial relationship between genomic DNA and time-dependent formation of replication foci or newly synthesized DNA (see fig. S7).

We demonstrated the significance of superresolution chromatin imaging in several settings of cancer research, which cannot be easily obtained from conventional microscopy. First, we explored molecular-scale chromatin structure, which showed gradual disruption of chromatin compaction that correlates with malignant transformation of colon carcinogenesis in the precancerous and cancerous tissues (Fig. 5). Next, to demonstrate the potential of superresolution chromatin imaging to gain more insights of the functional significance of chromatin compaction in malignant transformation, we explored the spatial relationship between DNA and the functionally important proteins associated with nuclear architecture—RNAPII and nuclear lamina. RNAPII is the transcriptional machinery that is directly regulated by chromatin organization, which showed progressively increased nanoclusters (Fig. 6) correlating with the increased transcriptional activities (1). Our two-color superresolution images of genomic DNA and active RNAPII showed significantly increased degree of colocalization between them, suggesting that the more open chromatin structure observed in the precancerous and cancer lesions was associated with the enhanced transcription activities. This result is consistent with our previous experiments performed in cells treated with siSUV39h1/h2 with more open chromatin structure, which showed markedly increased colocalization between genomic DNA and active RNAPII (1). Further inspired by our result of severely disrupted chromatin compaction at the nuclear periphery and well-known shape irregularity in cancer cells, we examined nuclear lamina as it connects the inner nuclear envelope and nuclear periphery. The superresolution images of nuclear lamina revealed gradually fragmented nuclear envelope at the nanoscale in precancerous and cancerous cells (Fig. 7). Our two-color superresolution images further revealed that disrupted nuclear lamina regions got closer to the fragmented chromatin nanodomains at the nuclear periphery in precancerous and cancer cells, and their nanodomain sizes were also correlated, supporting the previously reported physical association between LADs and the nuclear lamina (16, 17).

Last, we explored the feasibility of superresolution imaging of genomic DNA for cancer risk stratification in a proof-of-concept study in patients with well-defined cancer risk. Our results showed highly disrupted chromatin structure even in the normal-appearing epithelial cells in Lynch patients with a germline mutation of DNA mismatch repair genes with the past history of colorectal cancer, compared with those from healthy controls. However, a larger variation in chromatin compaction observed in Lynch patients without

a past history of cancer may be associated with their disease penetrance. This result shows the potential of superresolution imaging of chromatin compaction for cancer risk stratification even from nontumor cells.

Together, we demonstrated the small-molecule DNA-specific fluorophore Hoechst-Cy5 as a fast, simple, and robust DNA stain for high-quality superresolution chromatin imaging on clinically processed tissue samples. It significantly facilitates routine examination of superresolved chromatin structure from various pathological conditions directly on clinically processed tissue. We demonstrated the potential of superresolution chromatin imaging in providing new biological insights of nuclear architecture in malignant transformation and the use of nanoscale chromatin structure to risk-stratify patients at a higher risk for developing cancer. This approach opens new opportunities to explore the biological and clinical significance of superresolved chromatin structure for various diseases.

MATERIALS AND METHODS
Synthesis of Hoechst-Cy5
Hoechst-Cy5 was synthesized by Vanderbilt University Molecular Design and Synthesis Center. The schematics for synthesis route are described in fig. S1, and synthesis steps and validation are described in detail in the Supplementary Materials and Methods. The conjugable Hoechst analog was synthesized using the previously reported method (3). All chemicals and solvents were purchased from standard commercial sources. Dye purification and characterization were performed with semi-prep high-performance liquid chromatography, ^{1}H nuclear magnetic resonance, and liquid chromatography–mass spectrometry at Vanderbilt University.

DNA and immunofluorescence staining on mouse and human pathological tissue
For mouse tissue, all animal studies were performed in accordance with the institutional Animal Care and Use Committee at the University of Pittsburgh. Intestinal tissue from mice were fixed with 10% Neutral-Buffered Formalin Solution (Azer Scientific, catalog no. NBF-4-G) for 6 hours and then stored in 70% ethanol before embedding, followed by paraffin embedding at University of Pittsburgh Biospecimen Core as the standard tissue fixation method. Wild-type mouse was used for most DNA staining. For intestinal stem cell staining, we used an enhanced green fluorescent protein (EGFP)–labeled Lgr5 (Lgr5-EGFP-Ires-CreERT2) mouse (Jackson Laboratory) to examine the DNA structure of intestinal stem cells at the bottom of the crypt identified by Lgr5^{+} staining. GFP antibody was used to detect Lgr5 by immunostaining. The use of FFPE tissue blocks from deidentified patients was approved by the Institutional Review Board at the University of Pittsburgh. All tissues used in this study were formalin fixed and paraffin embedded accordingly to the standard clinical processing at University of Pittsburgh Medical Center.

All FFPE tissue blocks from both mouse and human tissue were sectioned at thickness of 3 μm and mounted on poly-D-lysine–coated coverslips. Tissue treatment before staining was followed by standard paraffinization and rehydration, antigen retrieval process (30). Briefly, after being heated for 30 min in 60°C oven, tissue sections were deparaffinized in xylene and rehydrated in graded ethanol and finally in water. Tissue sections were then washed in phosphate-buffered saline (PBS) and treated with 0.1% solution of sodium borohydride in PBS to reduce autofluorescence. Tissue sections were

then incubated with Hoechst-Cy5 (1 μM), Live-650 (1:1000 dilution from the original concentration, Biotium #40082), and Hoechst-JF646 (1 μM) for 1 hour at room temperature. Labeling density or staining concentration was optimized. For every dye, a standard concentration test was first conducted, and the optimal concentration was selected based on the following criteria: the bright fluorescence signal intensity in wide-field fluorescence images, the greatest localization density in individual clusters (nanodomains) in STORM images without introducing significant nonspecific binding outside the nucleus, and the low background signals from each imaging frame used for STORM image reconstruction. For TOTO-3 staining, tissues were first treated with deoxyribonuclease-free RNase (50 μg/ml) at 37°C for 30 min for RNase digestion and then incubated with 100 nM TOTO-3 for 1 hour at room temperature. After being washed three times in PBS, the fluorescent beads (FluoSpheres carboxylate, #F8803, Thermo Fisher Scientific) were deposited onto the coverslips as fiduciary markers used for drift correction based on our previously published method (31). The sample was ready for STORM imaging. STORM imaging buffer for tissue stained with different fluorescent probes was optimized for best blinking performance discussed previously such as fast photo-switching properties, high photon number per switching cycle, low on-off duty cycle, and low background (2). STORM imaging buffer for Hoechst-Cy5, Live-650, and Hoechst-JF646 consists of 60% 2,2-thiodiethanol (TDE) (v/v), 10% (w/v) glucose, glucose oxidase 0.14 M β-mercaptoethanol (0.56 mg/ml), and catalase (0.17 mg/ml). The same component, except β-mercaptoethanol, was used in TOTO-3 imaging.

For tissue samples costained with DNA with Hoechst-Cy5 and proteins with antibody, after deparaffinization and rehydration, antigen retrieval was conducted using Antigen Retriever from Electron Microscopy Sciences (catalog no. 62700-20) in eBioscience IHC Antigen Retrieval Solution (pH 9.0; catalog no. 00-4956-58). Tissue sections were blocked in 5% bovine serum albumin (BSA) for 1 hour at room temperature and then incubated with primary antibodies diluted to optimized concentrations at 4°C overnight: rabbit polyclonal to H3K4me3 (1:600; #07-473, Millipore), rabbit polyclonal to H3K9me3 (1:600; #ab8898, Abcam), mouse monoclonal to RNAP II (1:600; #ab5408, Abcam), mouse monoclonal to GFP (1:300; #sc-9996, Santa Cruz Biotechnology), CD3 (1:300; #ab35372, Abcam), and mouse anti–lamin A/C (1:300; #4777, Cell Signaling Technology). After washing, Hoechst-Cy5 and CF568-conjugated goat–anti-rabbit/mouse secondary antibody was applied to the sections at room temperature for 1 hour, protected from light. After being washed three times with PBS and deposition of fiduciary marker, the samples were ready for imaging.

DNA and immunofluorescence staining for cultured cells
U2OS cells were cultured in DMEM (Dulbecco's Modified Eagle Medium) supplemented with 10% fetal bovine serum. Cells were plated onto the Poly-D-lysine (PDL)-coated coverslips at an initial confluency of about 60 to 70% and cultured overnight to let the cells attach. After being washed once with PBS, cells were fixed with 4% paraformaldehyde and permeabilized with 0.2% Triton X-100 in PBS. DNA dyes with appropriate concentration (the same concentration was used as the tissue staining described above) diluted in PBS were incubated with the sample for 1 hour at room temperature. As described above in tissue staining, RNase digestion was required for TOTO-3 staining. After three times of washing with PBS and deposition of fiduciary marker, the samples were ready for STORM imaging.

DNA staining with EdU in cultured cells was performed by using the Click-iT Plus EdU Alexa Fluor Imaging Kit (Thermo Fisher Scientific, #C10340), as described previously (25). For fully DNA labeling, cells were incubated with medium containing 1 μM EdU for 24 hours, and after fixation and permeabilization, cells were blocked with 3% BSA and incubated with EdU Click-iT Plus reaction cocktail for 30 min following the manufacturer's instruction. DNA was detected by Azide Alexa-647.

For two-color staining of DNA and histone marks (H3K4me3), after being washed out of the reaction cocktail, cells were incubated with the primary antibody at 4°C overnight and secondary antibodies for 2 hours at room temperature. After being washed for three times with PBS and deposition of fiduciary marker, the samples were ready for STORM imaging.

For two-color staining of genomic DNA staining with Hoechst-Cy5 and replication foci staining with EdU, cells were incubated with the medium containing 1 μM EdU for a duration of 30 min, 1 hour, and 3 hours. After fixation and permeabilization, Azide CF-568 and Hoechst-Cy5 were diluted in the cocktail solution as described above and incubated with the cells for 1 hour at room temperature. Cells were ready for imaging after washing.

STORM imaging system
STORM images were acquired using our custom-built system on the Olympus IX71 inverted microscope frame with a 100×, numerical aperture of 1.4 oil immersion objective (UPLSAPO 100XO; Olympus), and the system has been described in detail previously (25, 31). For single-color dSTORM imaging, the excitation laser at 642 nm (VFL-P-1000-642-OEM3; MPB Communications, Point-Claire, Quebec, Canada) was used at power density of ~2.5 kW cm^{-2} for STORM imaging. The exposure time was 20 ms, and a total frame number of 30,000 were used. During the image acquisition, a small amount of activation power (~1 μW) for the 405-nm laser (DL405-050, CrystaLaser, Reno, NV) was added at the 20,001st frame, and the power of the 405-nm laser was gradually increased at a rate of 0.2% per 1000 frames. Two-color dSTORM imaging was conducted sequentially, where the first 30,000 frames were acquired on Hoechst-Cy5 with an exposure time of 20 ms for each frame, followed by 30,000 frames of CF-568 with the same exposure time. The excitation laser of 561 nm at laser power of 0.8 kW cm^{-2} (VFL-P-200-560-OEM1, MPB Communications, Point-Claire, Quebec, Canada) was used for imaging CF-568–immunolabeled targets. Drift correction was independently performed every 200 frames (or 4 s) with fluorescent beads (Thermo Fisher Scientific, F8803) excited with 488-nm laser (DL488-150, CrystaLaser, Reno, NV) as fiduciary markers throughout each image acquisition process, based on our established method (31). The imaging conditions (exposure time, power density, activation, and frame number) remain the same for all experiments reported in this study.

STORM image reconstruction and data analysis
The STORM images shown in Fig. 2 were reconstructed using ThunderSTORM ImageJ plugin, and the rest of the images were reconstructed by PathSTORM described in our previous publication (1). The analysis method of nanodomain size was calculated using the watershed method, and the degree of colocalization was described in our previous publications (1, 25) and briefed in the Supplementary Materials and Methods. The statistical comparison between two groups was calculated using nonparametric Mann-Whitney U

test in GraphPad Prism 9.0, and two-tailed *P* value at 95% confidence interval was presented throughout the manuscript.

To calculate nanodomain size, a Watershed segmentation algorithm was used to segment the individual localized nanodomains (or clusters) based on the reconstructed STORM images as described previously (*1*). In brief, the localized point list coordinates from single-molecule localization were first converted to a superresolution image with a pixel size of 13 nm. The algorithm then finds the regional intensity maxima of the STORM image, conducted using the "imregionalmax" function in MATLAB (MathWorks). The resultant binary map of maxima points was dilated using a disk-shaped kernel with a diameter of five pixels, and then a distance transform of the inverse dilated map was calculated using the "bwdist" function. The resultant distance map was amplified by a factor of 2 and then added to a binarized STORM image, which was then segmented using watershed function (built-in function in MATLAB). The examples of the watershed segmentation for the STORM images are shown in fig. S8.

To calculate degree of colocalization, we calculated the degree of colocalization (DoC) between DNA and other proteins by adapting a published Clus-DoC (*32*) software and was also described in our prior publication (*25*). In brief, for each localized spot from DNA, we first calculated the gradient density of DNA and a protein of interest (e.g., RNAPII) around this localized spot within circles of increasing radius (range of 20 to 500 nm at a step size of 10 nm used), respectively. This gradient density of DNA and a protein of interest was normalized by their respective gradient density within the area with the maximum radius and then used to calculate Spearman correlation.

SUPPLEMENTARY MATERIALS
Supplementary material for this article is available at https://science.org/doi/10.1126/sciadv.abm8293

View/request a protocol for this paper from *Bio-protocol*.

REFERENCES AND NOTES

1. J. Xu, H. Ma, H. Ma, W. Jiang, C. A. Mela, M. Duan, S. Zhao, C. Gao, E.-R. Hahm, S. M. Lardo, K. Troy, M. Sun, R. Pai, D. B. Stolz, L. Zhang, S. Singh, R. E. Brand, D. J. Hartman, J. Hu, S. J. Hainer, Y. Liu, Super-resolution imaging reveals the evolution of higher-order chromatin folding in early carcinogenesis. *Nat. Commun.* **11**, 1899 (2020).
2. G. T. Dempsey, J. C. Vaughan, K. H. Chen, M. Bates, X. Zhuang, Evaluation of fluorophores for optimal performance in localization-based super-resolution imaging. *Nat. Methods* **8**, 1027–1036 (2011).
3. A. Nakamura, K. Takigawa, Y. Kurishita, K. Kuwata, M. Ishida, Y. Shimoda, I. Hamachi, S. Tsukiji, Hoechst tagging: A modular strategy to design synthetic fluorescent probes for live-cell nucleus imaging. *Chem. Commun.* **50**, 6149–6152 (2014).
4. M. Ishida, H. Watanabe, K. Takigawa, Y. Kurishita, C. Oki, A. Nakamura, I. Hamachi, S. Tsukiji, Synthetic self-localizing ligands that control the spatial location of proteins in living cells. *J. Am. Chem. Soc.* **135**, 12684–12689 (2013).
5. G. Lukinavicius, C. Blaukopf, E. Pershagen, A. Schena, L. Reymond, E. Derivery, M. Gonzalez-Gaitan, E. D'Este, S. W. Hell, D. Wolfram Gerlich, K. Johnsson, SiR-Hoechst is a far-red DNA stain for live-cell nanoscopy. *Nat. Commun.* **6**, 8497 (2015).
6. J. Bucevicius, J. Keller-Findeisen, T. Gilat, S. W. Hell, G. Lukinavicius, Rhodamine-Hoechst positional isomers for highly efficient staining of heterochromatin. *Chem. Sci.* **10**, 1962–1970 (2019).
7. C. K. Spahn, M. Glaesmann, J. B. Grimm, A. X. Ayala, L. D. Lavis, M. Heilemann, A toolbox for multiplexed super-resolution imaging of the E. coli nucleoid and membrane using novel PAINT labels. *Sci. Rep.* **8**, 14768 (2018).
8. W. R. Legant, L. Shao, J. B. Grimm, T. A. Brown, D. E. Milkie, B. B. Avants, L. D. Lavis, E. Betzig, High-density three-dimensional localization microscopy across large volumes. *Nat. Methods* **13**, 359–365 (2016).
9. J. B. Grimm, B. P. English, J. Chen, J. P. Slaughter, Z. Zhang, A. Revyakin, R. Patel, J. J. Macklin, D. Normanno, R. H. Singer, T. Lionnet, L. D. Lavis, A general method to improve fluorophores for live-cell and single-molecule microscopy. *Nat. Methods* **12**, 244–250 (2015).
10. L. Xiang, K. Chen, R. Yan, W. Li, K. Xu, Single-molecule displacement mapping unveils nanoscale heterogeneities in intracellular diffusivity. *Nat. Methods* **17**, 524–530 (2020).
11. M. Ovesný, P. Křížek, J. Borkovec, Z. Švindrych, G. M. Hagen, ThunderSTORM: A comprehensive ImageJ plug-in for PALM and STORM data analysis and super-resolution imaging. *Bioinformatics* **30**, 2389–2390 (2014).
12. M. A. Ricci, C. Manzo, M. F. García-Parajo, M. Lakadamyali, M. P. Cosma, Chromatin fibers are formed by heterogeneous groups of nucleosomes in vivo. *Cell* **160**, 1145–1158 (2015).
13. J. H. Bushweller, Targeting transcription factors in cancer—From undruggable to reality. *Nat. Rev. Cancer* **19**, 611–624 (2019).
14. N. Laham-Karam, G. P. Pinto, A. Poso, P. Kokkonen, Transcription and translation inhibitors in cancer treatment. *Front. Chem.* **8**, 276 (2020).
15. C. Denais, J. Lammerding, Nuclear mechanics in cancer, in *Cancer Biology and the Nuclear Envelope: Recent Advances May Elucidate Past Paradoxes*, E. C. Schirmer, J. I. de las Heras, Eds. (Springer New York, New York, NY, 2014), pp. 435–470.
16. K. L. Reddy, J. M. Zullo, E. Bertolino, H. Singh, Transcriptional repression mediated by repositioning of genes to the nuclear lamina. *Nature* **452**, 243–247 (2008).
17. J. M. Zullo, I. A. Demarco, R. Piqué-Regi, D. J. Gaffney, C. B. Epstein, C. J. Spooner, T. R. Luperchio, B. E. Bernstein, J. K. Pritchard, K. L. Reddy, H. Singh, DNA sequence-dependent compartmentalization and silencing of chromatin at the nuclear lamina. *Cell* **149**, 1474–1487 (2012).
18. S. F. Moss, V. Krivosheyev, A. de Souza, K. Chin, H. P. Gaetz, N. Chaudhary, H. J. Worman, P. R. Holt, Decreased and aberrant nuclear lamin expression in gastrointestinal tract neoplasms. *Gut* **45**, 723–729 (1999).
19. Z. Wu, L. Wu, D. Weng, D. Xu, J. Geng, F. Zhao, Reduced expression of lamin A/C correlates with poor histological differentiation and prognosis in primary gastric carcinoma. *J. Exp. Clin. Cancer Res.* **28**, 8 (2009).
20. E. J. T. Belt, R. J. A. Fijneman, E. G. van den Berg, H. Bril, P. M. Delis-van Diemen, M. Tijssen, H. F. van Essen, E. S. M. de Lange-de Klerk, J. A. M. Beliën, H. B. A. C. Stockmann, S. Meijer, G. A. Meijer, Loss of lamin A/C expression in stage II and III colon cancer is associated with disease recurrence. *Eur. J. Cancer* **47**, 1837–1845 (2011).
21. B. van Steensel, A. S. Belmont, Lamina-associated domains: Links with chromosome architecture, heterochromatin, and gene repression. *Cell* **169**, 780–791 (2017).
22. G. D. Guler, C. A. Tindell, R. Pitti, C. Wilson, K. Nichols, T. KaiWai Cheung, H. J. Kim, M. Wongchenko, Y. Yan, B. Haley, T. Cuellar, J. Webster, N. Alag, G. Hegde, E. Jackson, T. L. Nance, P. G. Giresi, K. B. Chen, J. Liu, S. Jhunjhunwala, J. Settleman, J.-P. Stephan, D. Arnott, M. Classon, Repression of stress-induced LINE-1 expression protects cancer cell subpopulations from lethal drug exposure. *Cancer Cell* **32**, 221–237.e13 (2017).
23. D. Provenzale, S. Gupta, D. J. Ahnen, T. Bray, J. A. Cannon, G. Cooper, D. S. David, D. S. Early, D. Erwin, J. M. Ford, F. M. Giardiello, W. Grady, A. L. Halverson, S. R. Hamilton, H. Hampel, M. K. Ismail, J. B. Klapman, D. W. Larson, A. J. Lazenby, P. M. Lynch, R. J. Mayer, R. M. Ness, S. E. Regenbogen, N. J. Samadder, M. Shike, G. Steinbach, D. Weinberg, M. Dwyer, S. Darlow, Genetic/familial high-risk assessment: Colorectal version 1.2016, NCCN clinical practice guidelines in oncology. *J. Natl. Compr. Cancer Netw.* **14**, 1010–1030 (2016).
24. P. J. Zessin, K. Finan, M. Heilemann, Super-resolution fluorescence imaging of chromosomal DNA. *J. Struct. Biol.* **177**, 344–348 (2012).
25. J. Xu, H. Ma, J. Jin, S. Uttam, R. Fu, Y. Huang, Y. Liu, Super-resolution imaging of higher-order chromatin structures at different epigenomic states in single mammalian cells. *Cell Rep.* **24**, 873–882 (2018).
26. H. Miller, Z. Zhou, A. J. M. Wollman, M. C. Leake, Superresolution imaging of single DNA molecules using stochastic photoblinking of minor groove and intercalating dyes. *Methods* **88**, 81–88 (2015).
27. C. Flors, Super-resolution fluorescence imaging of directly labelled DNA: From microscopy standards to living cells. *J. Microsc.* **251**, 1–4 (2013).
28. A. T. Szczurek, K. Prakash, H. K. Lee, D. J. Zurek-Biesiada, G. Best, M. Hagmann, J. W. Dobrucki, C. Cremer, U. Birk, Single molecule localization microscopy of the distribution of chromatin using Hoechst and DAPI fluorescent probes. *Nucleus* **5**, 331–340 (2014).
29. E. Eiseman, S. B. Haga, *Handbook of Human Tissue Sources: A National Resource of Human Tissue Samples* (RAND Corporation, Santa Monica, CA, 1999).
30. J. Xu, H. Ma, Y. Liu, Optimized stochastic optical reconstruction microscopy for imaging chromatin structure in pathological tissue. *Curr. Protoc. Cytom.* **94**, e78 (2020).
31. H. Ma, J. Xu, J. Jin, Y. Huang, Y. Liu, A simple marker-assisted 3D nanometer drift correction method for superresolution microscopy. *Biophys. J.* **112**, 2196–2208 (2017).
32. S. V. Pageon, P. R. Nicovich, M. Mollazade, T. Tabarin, K. Gaus, Clus-DoC: A combined cluster detection and colocalization analysis for single-molecule localization microscopy data. *Mol. Biol. Cell* **27**, 3627–3636 (2016).